Research Article | Vol. 2, No. 12 / 15 December 2019 / OSA Continuum 3521

Time-domain spectroscopy of $KTiOPO_4$ in the frequency range 0.6–7.0 THz

KJELL MARTIN MØLSTER,[1,2,*] TRYGVE SØRGÅRD,[3] HUGO LAURELL,[4] CARLOTA CANALIAS,[1] VALDAS PASISKEVICIUS,[1] FREDRIK LAURELL,[1] AND ULF ÖSTERBERG[1,2]

[1]*Department of Applied Physics, Royal Institute of Technology, KTH, 10691 Stockholm, Sweden*
[2]*Department of Electronic Systems, Norwegian University of Natural Science and Technology, N-7491 Trondheim, Norway*
[3]*Department of Physics, Norwegian University of Science and Technology, Trondheim NO-7491, Norway*
[4]*Division of Atomic Physics at the Faculty of Engineering (LTH), Lund University, Lund, Sweden*
[*]*moelster@kth.se*

Abstract: We report on THz time-domain spectroscopy measurements of flux grown $KTiOPO_4$ in the frequency range 0.6–7.0 THz (20 to 240 cm^{-1}). Our results compare well with earlier Raman and far-infrared measurements. We theorize that the differences between the optical phonon mode resonances reported in the literature are due to what growth parameters and melt compositions are used to grow the crystals. We also report on a new feature at 1.4 THz (47 cm^{-1}).

1. Introduction

Functional oxide materials are of great interest for applications in electronics, spintronics and photonics due to their optical, magnetic and electrical properties and their abilities to be engineered for use in devices. Within this group, the class of complex oxides with the structure ABO_3, have been used to produce memory and spin electronics devices via strain induced ferromagnetism [1,2]. For nonlinear and electro-optical applications Lithium Niobate ($LiNbO_3$) was investigated as early as in the 1960's [3]. Later, Barium Titanate ($BaTiO_3$) was recognized for its use in data processing [4] and Potassium Titanyl Phosphate ($KTiOPO_4$, KTP) for its electro-optical and dielectric properties [5]. KTP, due to its high nonlinear coefficient, high damage threshold, and large transparency window was also acknowledged early on for use in second-harmonic generation (SHG) and optical parametric oscillators [6]. Furthermore, because of its ferroelectric properties it has been shown that the nonlinear conversion efficiency can be increased by exploiting quasi-phasematching (QPM) where a periodic domain structure is imprinted in the crystal by electric field poling of the crystal [7,8]. Another important application today is in quantum optics where light sources with entangled photons are needed. These can also be efficiently made today with periodically poled nonlinear crystals [9–11]. Also quantum memories have been demonstrated in waveguide structures of both Lithium Niobate and KTP [12].

Recent interest in THz systems [13–15] for use in manufacturing, quality control, medical imaging and security monitoring - to name a few - has prompted a need for efficient and affordable generation of THz radiation. In this frequency regime KTP appears to be a good option by e.g. using it's quasi-phase matching properties in optical parametric amplifiers [16,17], or as envisaged in [18], pumped with a dual wavelength fiber laser for direct THz conversion through the beat frequency [19]. Recently, THz generation using parametric amplification in KTP was observed [20], and very recently Wu et al. demonstrated generation of >100 kW peak power from a KTP THz parametric oscillator [21].

With the increased attention to possible KTP THz devices there is additional need for spectroscopic data. The crystallographic structure and chemical formula of KTP was first

#378058 https://doi.org/10.1364/OSAC.2.003521
Journal © 2019 Received 23 Sep 2019; revised 31 Oct 2019; accepted 3 Nov 2019; published 12 Dec 2019

OSA CONTINUUM

reported in 1974 [22]. Later studies investigated crystal properties and linear and nonlinear optical characteristics [23–28]. Studies directly aimed at optical absorption and reflectivity in the far-infrared regime were undertaken by the groups of Wyncke and Kugel in the 1980's and 1990's [29–31]. They performed both Raman and IR measurements between 15 to 4000 cm^{-1} to capture most of the A_1, A_2, B_1, and B_2 optical phonon modes. A study in 1996 showed the effect of the choice of flux used in flux grown KTP on the different vibrational modes [32]. A study by Watson in 1991 [33], compared flux grown $KTiOAsO_4$ (KTA) with hydrothermally grown KTP to provide insight into the importance of the $Ti - O$ bond in the Raman spectra. Later studies focusing on the THz frequency region using femtosecond lasers for long wavelength radiation reported KTP absorption for 0.1 – 1.5 THz [34], 0.5 – 2.0 THz [35] and 0.2 – 2.6 THz [16]. These studies were all performed in transmission and therefore limited to ca 2.5 THz due to the strong increase in absorption for higher frequencies and low amplitude at higher frequencies afforded by standard THz sources. A very different approach for resolving fine spectral features in the optical phonon modes of KTP was performed by Card and co-workers [36] using ultrafast CARS. They investigated the region 640 to 850 cm^{-1} (ca. 19 – 25 THz).

In this study coherent femtosecond THz pulses in reflection and transmission were used to study optical phonons in flux-grown KTP between 0.6 - 7.0 THz to lay additional groundwork for the fabrication of KTP based THz devices.

2. Experiment

2.1. THz generation and detection

The experimental setup is shown in Fig. 1, THz radiation was generated from a two-color self-induced air plasma using an amplified Ti:Sapphire laser system (Spectra-Physics, Solstice) [37,38]. The fundamental beam at 795 nm was focused with a f =250 mm lens. Immediately after the lens, a 100 µm thick BBO crystal was positioned to frequency double the fundamental wave. The focused beams produced a ca. 5 mm long plasma. The near-IR laser had an average power of 1.7 W, a repetition rate of 1 kHz and a pulse width of 90 fs. The THz radiation was collected and collimated using a 50.8 mm focal length off-axis paraboloidal mirror. The fundamental wavelength was removed using a 1 mm thick, NIR-THz spectral splitter (TYDEX), Silicon wafer. The THz beam was chopped using a mechanical chopper and polarized by a HDPE polarizer (TYDEX). The THz was focused onto the sample/reference using a 100 mm off-axis paraboloidal mirror. The f =100 mm mirror had a 1 mm hole drilled through it, such that the probe beam collinearly propagated with the THz radiation before impinging on the sample/reference at an incident angle of 45° [39]. A 300 µm thick Gallium Phosphide (GaP) electro-optic crystal was positioned close to the sample/reference surface to capture as much of the reflected light as possible. After the GaP crystal, the probe beam propagated ca. 1 m to a (Zomega) balanced differential detector. The long distance between the GaP crystal and the detector was to simplify the removal of the reflected probe beam from the back surface of the KTP crystal using spatial filtering. The signal from the balanced differential detector was sent to a lock-in amplifier (SR830) which was connected to a computer. A MATLAB data acquisition program was used to move the translation stage for the probe beam and collect data from the lock-in amplifier.

A typical reflection trace for s-polarized light in the crystallographic a-direction of KTP is shown in Fig. 2, together with its reference from a gold mirror [40]. Transmission measurements were performed by inserting the sample in the collimated portion of the THz beam and reflecting off from the same gold reference as used in the reflectivity measurements, Fig. 1.

The dynamic range (DR) was estimated by comparing the peak of the time signal to the noise floor far away from the peak, and was estimated to >1000 : 1 for all measurements. Furthermore, the frequency dependent DR follows the Fourier transformed time signals as described in [41], and can be used to estimate the limits of the measurements (e.g α_{max} for transmission). This

OSA CONTINUUM

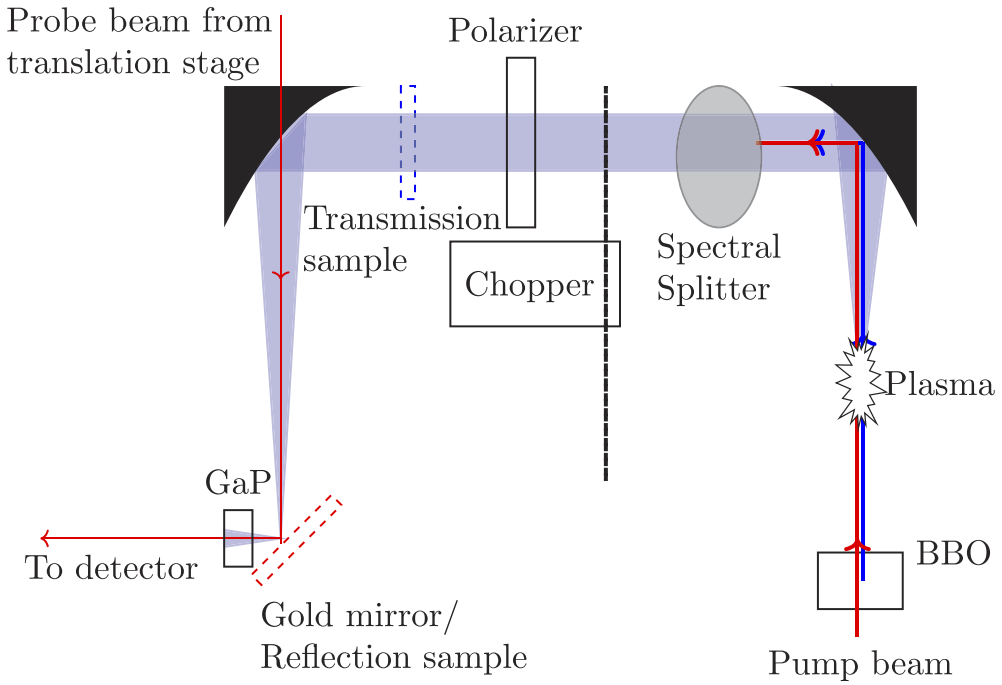

Fig. 1. Experimental setup. The red dashed rectangle shows the position of the gold mirror and the sample in reflection mode. The angle of incidence is 45°. The dashed blue rectangle shows the position of the sample in transmission mode. The red, blue and shaded lines are the fundamental, second-harmonic and THz beam, respectively.

upper limit - α_{max} - of a transmission measurement manifests itself as a saturation of the refractive index and absorption coefficient, as seen in Fig. 6–9.

The analysis of the data was performed by first multiplying the raw time trace with an Airy window ($Ai(|x|^2 - 1)$, FWHM$\approx$ 6.8 ps) to remove the ringing in the frequency spectrum from the experimentally imposed boxcar window. Airy windowing is suitable since it is a compromise between a boxcar window (no smoothing) and a Gaussian window (strong smoothing). The resolution in frequency was $\approx$ 90 GHz or $\lesssim 2\,\mathrm{cm}^{-1}$, limited by our scan length of 11 ps. The limited length of the time scan was dictated by the Fabry-Pérot echoes present in our setup. We are unable to filter out these echoes without affecting the spectrum.

The transfer function $H(\omega)$ is defined as;

$$H(\omega) = \frac{E_s(\omega)}{E_r(\omega)} = |H(\omega)|e^{i\varphi(\omega)} \tag{1}$$

where $|H(\omega)|$ is the amplitude and $\varphi(\omega)$ is the phase. In Fig. 3 we show the spectra for the reflection signals from the sample $E_s(\omega)$ and the reference $E_r(\omega)$ for the time signals in Fig. 2. Figure 3 also includes a transmission measurement, illustrating the difficulty of performing absorption measurements of KTP in transmission. For the transmission spectrum shown in yellow, a longer time scan was used to bring out the spectral features around 4 THz. The noise floor and the spectral modulation of this spectrum is a product of increased resolution and Fabry-Pérot echoes from the EO-crystal. It compares well with the absorption window for the reflection signal in Fig. 5

OSA CONTINUUM

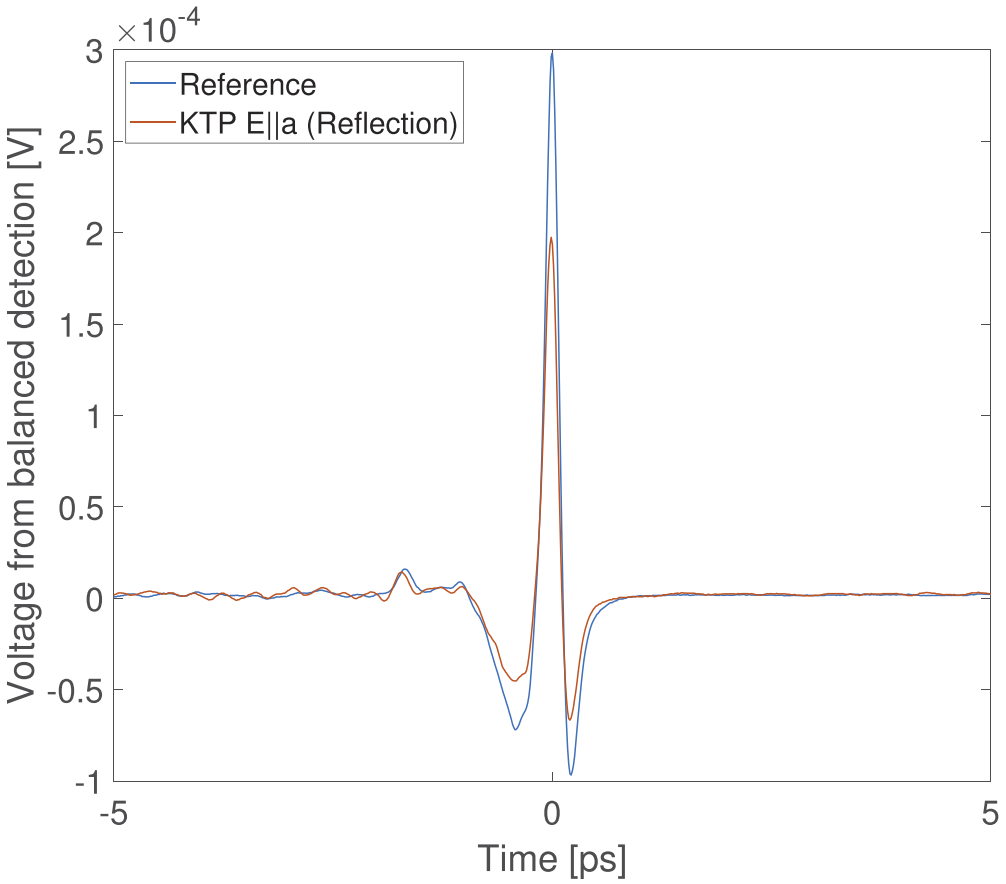

Fig. 2. The measured time trace for a single-cycle THz wave reflecting off; (orange) the KTP sample in the crystallographic a-direction and (blue) the gold mirror reference. The vertical axis is in units of volts and represent the output from the lock-in amplifier.

2.2. Measurement errors

In our reflectivity setup we removed the systematic phase error, due to the displacement between the sample and reference positions, using a configuration similar to that reported by Pashkin [39]. A side effect of this configuration is that the power ratio for the reflected probe beam off the sample and the reference needs to be measured accurately for the absolute values of the refractive index and the absorption coefficient to be valid. IR probe power (< 1mW) measurements were accurate to better than 1%. The reflectivity data are substantiated by the transmission measurements in the 0.6 – 2 THz region where it is not limited by absorption (α_{max}[41]). Random errors from our measurements were estimated from the standard deviation of the noise floor for each of the spectra. The errors $r = r_{avg} \pm \Delta_r$ and $\varphi = \varphi_{avg} \pm \Delta_\varphi$ were calculated using the formalism in [43,44]. The errors in the amplitude and phase resulted in the following errors, Δn and $\Delta\alpha$ for the calculated refractive index n and the absorption coefficient α in the frequency regions; (i) 0.6 – 3 THz, $\Delta n < \pm 0.025$ and $\Delta\alpha < \pm 5\,\mathrm{cm}^{-1}$; (ii) 3 – 5 THz, $\Delta n < \pm 0.05$ and $\Delta\alpha < \pm 25\,\mathrm{cm}^{-1}$; (iii) 5 – 6 THz, $\Delta n < \pm 0.1$ and $\Delta\alpha < \pm 50\,\mathrm{cm}^{-1}$; (iv) 6 – 7 THz, $\Delta n < \pm 0.25$ and $\Delta\alpha < \pm 150\,\mathrm{cm}^{-1}$.

OSA CONTINUUM

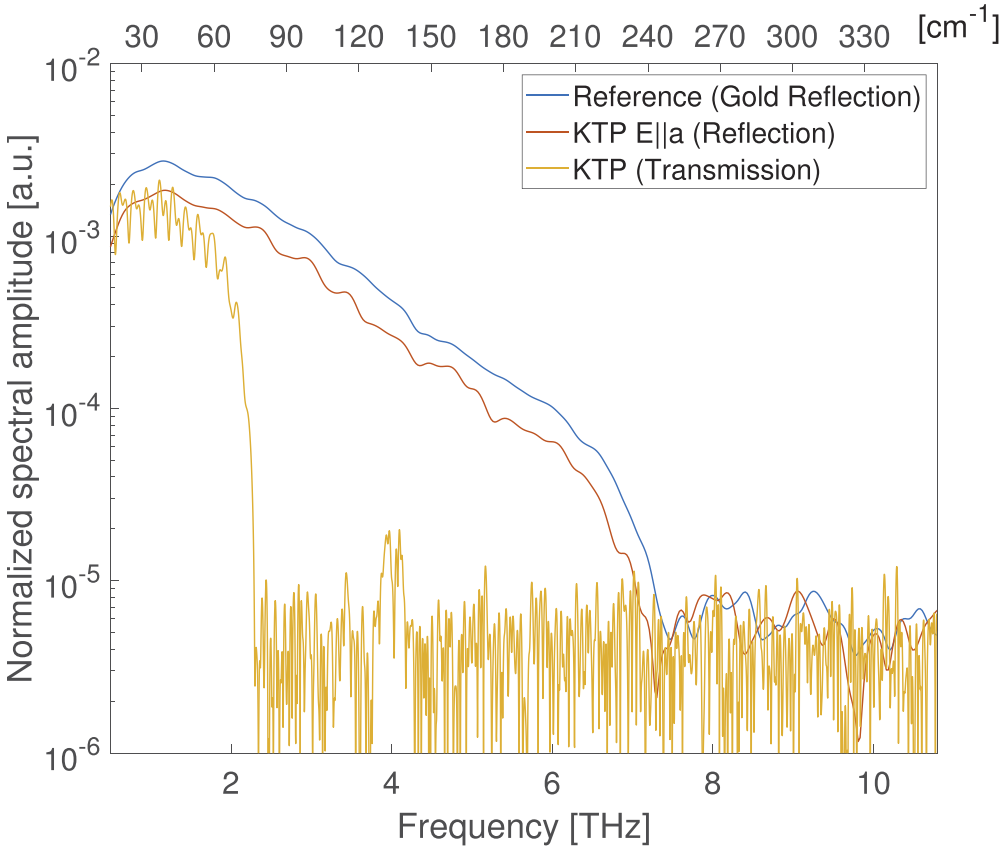

Fig. 3. The Fourier spectra from the time traces in Fig. 2. An additional transmission spectrum (yellow) of KTP, from [42], showing the strong absorption of THz in KTP. Note the band of transparency around 4 THz.

2.3. Sample

A flux grown, single domain KTP wafer was cut into samples with dimensions of 25 mm, 15 mm and 1 mm along the a, b, c crystallographic axes, respectively. The sample polar surfaces, parallel to the c-axis were polished to optical finish and cleaned using acetone. No other chemicals were used on the surface. The measured ionic conductivity of the sample was constant along the crystallographic b-direction. In the a-direction, it varied in a parabolic manner, being one order of magnitude larger in the center than at the edges. All of our measurements were performed in the same region, in the middle of the sample, where the conductivity was larger [45]. Figure 4 shows the geometry of the sample in relationship to the crystallographic directions and the polarization of the THz beam. The THz photons were always s-polarized when impinging on the surface of the sample or the reference. The laboratory frame is indicated by x, y, z.

Following the paper by Kugel [30] we use both the Porto notation $k_i(e_i, e_s)k_s$, [46] and, the polarization direction, e.g. E || a for easier comparison between results from other publications. In the Porto notation $k_{i,s}$ represent the incoming and scattered directions of propagation, respectively, and $e_{i,s}$ are the directions of polarization of the incoming and scattered beams, respectively. The polarization notation, e.g. E || a, indicates that the polarization direction of the field E is along the crystal direction a. Group theoretical analysis of the KTP point group, C_{2v} (mm2) distinguishes different symmetry vibrational modes corresponding to the irreducible representations A_1, A_2,

OSA CONTINUUM

Table 1. Optical phonon modes of B_1 and A_1 symmetry. The P indicates flux grown KTP using Phosphate, T indicates flux grown KTP using Tungstate. The bold numbers are shown with blue lines in Fig. 5

this work [cm^{-1}]	from [30] B_1 [cm^{-1}]	from [32] P [cm^{-1}]	from [32] T [cm^{-1}]	from [30] A_1 [cm^{-1}]	from [33] [cm^{-1}]
47	-	-	-	-	-
60	-	58	58	-	58
69	74	72	71	-	-
82	80	77	-	79	-
-	84	-	-	-	88
-	89	-	89	91	93
-	-	-	-	95	97
101	103	-	102	-	102
-	-	-	-	111	114
116	119	116	119	118	-
-	-	-	-	122	-
-	-	-	-	129	-
131	133	130	-	134	133
141	139	144	-	145	-
160	159	-	154	154	154
170	171	168	165	167	168
185	-	180	-	179	179
-	-	197	195	-	-
204	-	-	202	204	203
212	210	210	-	213	214
222	221	219	-	-	-
232	-	231	230	-	231
240	-	-	-	235	243

B_1, and B_2. Our experimental setup was configured to measure B_1 modes (E || a, i.e. z(aa)x) and B_2 modes (E || b, i.e. z(bb)x).

OSA CONTINUUM

Table 2. Optical phonon modes of B_2 symmetry. The P indicates flux grown KTP using Phosphate, T indicates flux grown KTP using Tungstate. The bold numbers are shown with orange lines in Fig. 5

this work [cm^{-1}]	from [30] [cm^{-1}]	from [32] P [cm^{-1}]	from [32] T [cm^{-1}]	from [33] [cm^{-1}]
62	-	58	58	-
72	75	72	71	-
-	80	77	-	88
92	92	-	89	91
105	104	-	102	103
115	116	116	119	115
125	123	-	-	123
-	128	130	-	-
144	145	144	-	-
-	151	-	-	-
155	157	-	154	157
-	-	168	165	-
-	175	-	-	172
186	181	180	-	179
-	-	197	195	-
203	202	-	202	202
213	-	210	-	-
222	221	219	-	221
-	231	231	230	232

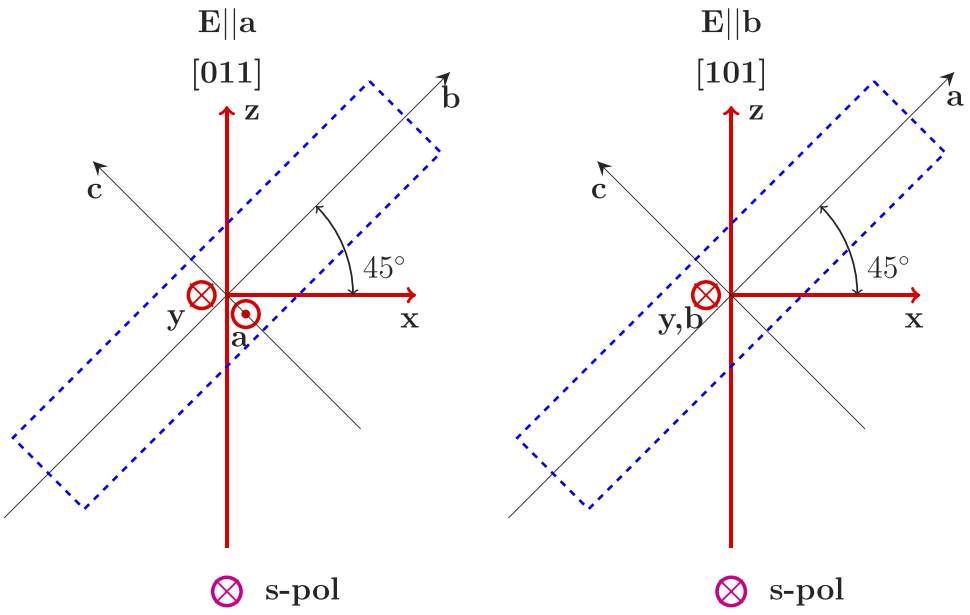

Fig. 4. Sample configuration for measuring (LEFT) B_1 modes (E || a or z(aa)x), and (RIGHT) B_2 modes (E || b or z(bb)x). The crystallographic plane is related to the laboratory frame through the z-direction. The impinging radiation is always s-polarized and the angle of incidence is 45-degrees.

OSA CONTINUUM

3. Results and discussion

We use reflection and transmission measurements to extract the real and imaginary parts of the refractive index, $\tilde{n}(\omega) = n(\omega) + i\kappa(\omega)$. Where κ is related to the absorption coefficient $\alpha = 2\frac{\omega}{c}\kappa$, [$cm^{-1}$]. The transmission values are limited to 2 THz due to large absorption (α_{max}[41]) and none of the measurements are accurate below 0.6 THz due to instrumentation errors.

3.1. Attenuation

In transmission, the extinction coefficient may be calculated as,

$$\kappa(\omega) = -\frac{c}{\omega d}\log\left[\frac{(n(\omega)+n_{air})^2}{4n(\omega)}|H(\omega)|\right] \tag{2}$$

for a (thick) sample where d represents the sample thickness, $|H(\omega)|$ is defined by Eq. 1, and $n(\omega)$ is calculated from Eq. 4.

In reflection, for an incidence angle of 45° and s-polarization, we use the formula,

$$\kappa(\omega) = \frac{\sqrt{2}|H(\omega)|\sin(\varphi(\omega))}{1+|H(\omega)|^2-2|H(\omega)|\cos(\varphi(\omega))}\frac{1}{\sqrt{1-\frac{1}{2n(\omega)^2}}} \tag{3}$$

derived in, e.g. [42]. Here, $|H(\omega)|$ and $\varphi(\omega)$ is defined by Eq. 1, and $n(\omega)$ is calculated from Eq. 5.

In Fig. 5, for comparison, we show the absorption, for the two cases, when the THz field is polarized along both the a and b crystal directions between 0.6 – 7 THz, demonstrating that there are strong peaks of absorption for frequencies above 2 THz which prevent reliable measurements using transmission spectroscopy. The reflection measurements show that there are broad frequency regions with much lower loss permitting electromagnetic wave propagation. For comparison we have summarized our data with those in the literature in Tables 1 and 2. These show the many overlapping phonon resonances between KTP crystals grown under different conditions, where the association of the resonances from different studies is made as judiciously as possible.

In Fig. 6 we show both transmission and reflection data for the B_1 , z(aa)x, symmetry excitation. For this measurement, we noticed a small vertical tilt (<1°) of the sample. This provided us with another excitation, z(cc)x, corresponding to A_1 modes. It may seem that the projection onto the c-direction, from such a small tilt, is insignificant. However, we observe a similar increase in absorption, from A_1 modes in the 1-2 THz region, as reported in [16]. This could explain the small discrepancy in absorption between reflection and transmission measurements, since this sample tilt was not present in the transmission measurements. By further comparison with other published peaks in Table 1, we surmise that we also observe some of the higher frequency A_1 modes for the reflection measurement. We verified that there is no contribution from A_1 modes into the B_2 measurements.

Our measured absorption peaks compare well with the measurements in [11,16,30,32–34]. The peak around 1.7 THz (≈60 cm^{-1}) has, in addition to these measurements, been observed for both flux grown KTP by [11,16,32] and for hydrothermally grown KTP by [33]. This peak has only been observed for A_1 symmetry and c excitations. Note that Vivekanandan [32] used pulverized KTP so all directions were excited simultaneously. This peak has been suggested to be either part of the Ti-O vibrations responsible for many of the <200 cm^{-1} peaks [33] or from a crystal sublattice [16]. The broad feature we observe around 1 THz was also reported by [16] and they speculated that it had also been observed by [34]. The peak around 1.4 THz (≈47 cm^{-1}) which we observe has not previously been reported in KTP. A peak close to that frequency has been reported for flux-grown KTA, [33]. Watson speculates that the 58 cm^{-1} peak in KTP

OSA CONTINUUM

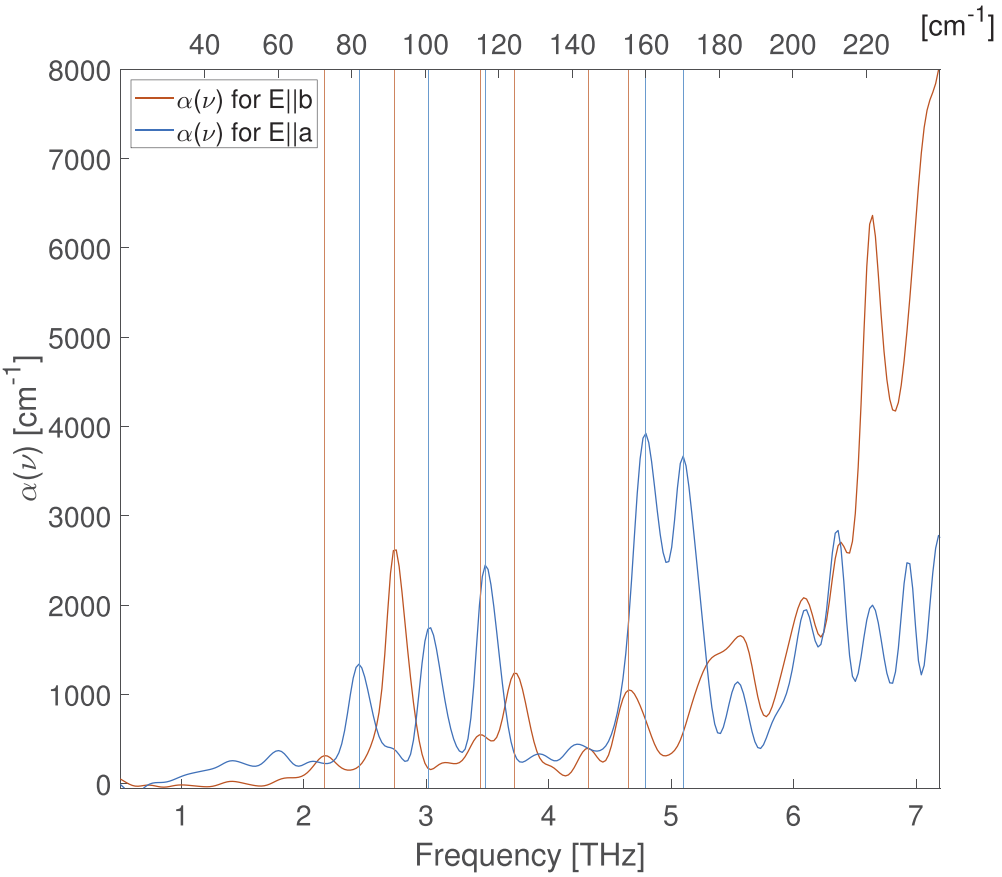

Fig. 5. The absorption coefficient for both (blue) B_1 modes (E || a) and (orange) B_2 modes (E || b) measured by reflection spectroscopy. Additional lines, with the identicalcode, illustrate a few select resonances frequencies found in bold font in Tables 1 and 2

is due to a Ti-O soft mode and due to the smaller distortion of the TiO_6 octahedron in KTA compared with KTP, that soft mode has a peak at 41 cm^{-1} in KTA. Since we observe both peaks it seems questionable that both modes are due to the same Ti-O vibration. More spectroscopic measurements on KTP crystals with known growth parameters and melt compositions are needed to better assign phonon resonances to specific bonds in the crystal and to explain why certain resonances are absent in some samples.

Similarly, in Fig. 7 we show transmission and reflection for the B_2 symmetry. This polarization direction has 12 resonances between $1 - 7$ THz compared with 16 for the A_1, B_1 directions. Here we notice that the reflection measurements give an apparent negative absorption value between $0.6 - 1.7$ THz. The reason is that the absorption is so small that the reflection measurement becomes unreliable for these frequencies.

3.2. Refractive index

The refractive index was calculated from the measured transmission data using

$$n(\omega) = \frac{\varphi(\omega)c}{\omega d} + n_{air} \tag{4}$$

OSA CONTINUUM

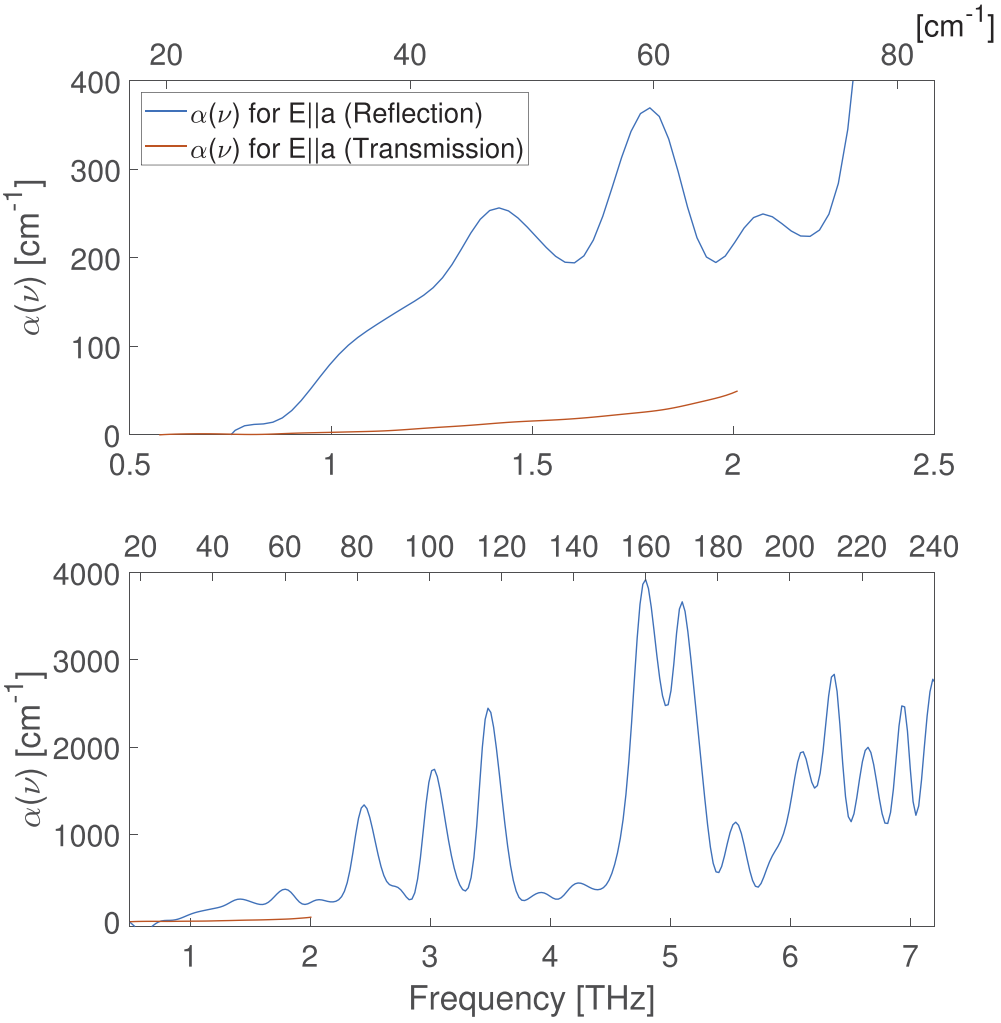

Fig. 6. Absorption coefficient for phonon modes with B_1 and A_1 symmetry measured by (orange) transmission and (blue) reflection measurements. The saturation due to high absorption in transmission can be seen at around 2 THz. (TOP) Absorption coefficient from 0.6 to 2.5 THz. (BOTTOM) Absorption coefficient from 0.6 to 7 THz.

OSA CONTINUUM

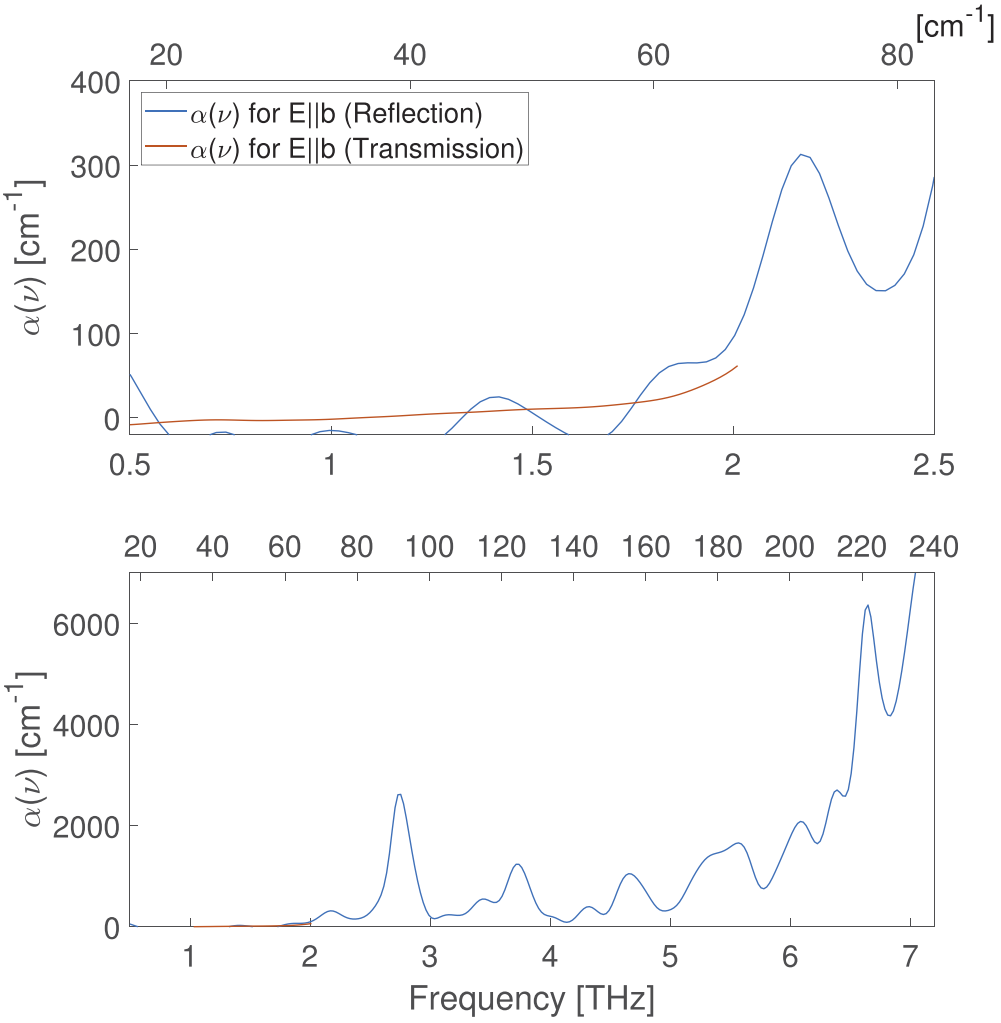

Fig. 7. Absorption coefficient for phonon modes with B_2 symmetry measured by (orange) transmission and (blue) reflection measurements. The saturation due to high absorption in transmission can be seen at around 2 THz. (TOP) Absorption coefficient from 0.6 to 2.5 THz. (BOTTOM) Absorption coefficient from 0.6 to 7 THz.

OSA CONTINUUM

and for the reflection data (at 45 °) using

$$n(\omega) = \sqrt{\frac{(1 - |H(\omega)|^2)^2}{2(1 + |H(\omega)|^2 - 2|H(\omega)|\cos(\varphi(\omega)))^2} + 1} \tag{5}$$

Figure 8 shows the refractive index for the B_1 measurements. We observe a discrepancy between the reflection and transmission measurements in the 1-2 THz region. We contend that this is again due to the tilt of the sample, which accounts for the higher refractive index due to the contributions from the A_1 modes [16], for the reflection measurement.

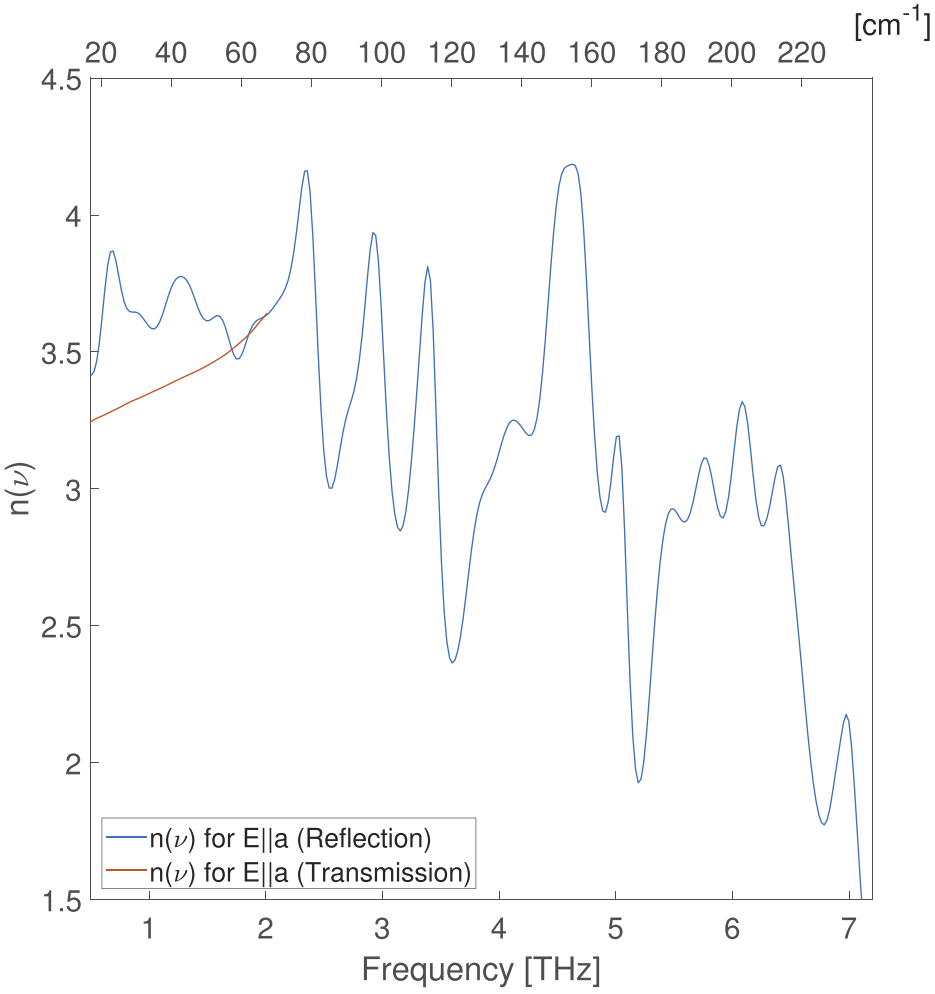

Fig. 8. Refractive index for phonon modes of B_1 and A_1 symmetry measured by (orange) transmission and (blue) reflection measurements. The saturation due to high absorption in transmission can be seen at around 2 THz.

Figure 9 shows that the refractive index for the B_2 modes compare favourably between transmission and reflection measurements in the 1-2 THz region.

OSA CONTINUUM

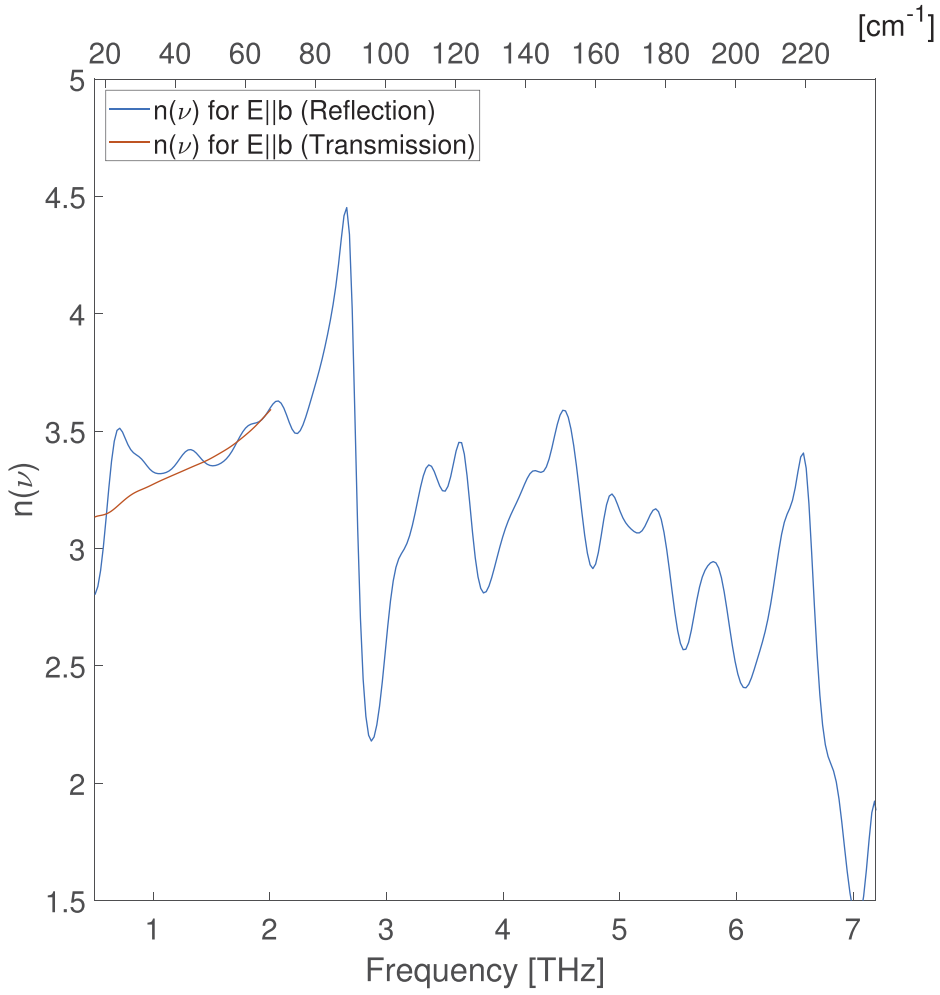

Fig. 9. Refractive index for phonon modes of B_2 symmetry measured by (orange) transmission and (blue) reflection measurements. The saturation due to high absorption in transmission can be seen at around 2 THz.

3.3. *Analysis*

In order to estimate the properties of the measured resonances, a least-squares fit was used, similar to the work by Kugel [30]. The data was fit to the Lorentz function

$$\varepsilon(\omega) = \varepsilon_\infty + \sum_{n=1}^{N} \Delta\varepsilon_n \frac{\omega_{0,\,n}^2}{\omega_{0,\,n}^2 - i\omega\Gamma_n - \omega^2}. \tag{6}$$

using $3N + 1$ independent variables; the high-frequency permittivity ε_∞, as well as the resonance frequency $\omega_{0,\,n}$, damping constant Γ_n and oscillation strength $\Delta\varepsilon_n$ for each of the N poles. The initial guesses for the resonance frequencies were taken from this work in Tables 1 and 2. The least-squares fit was weighted using the calculated errors such that more emphasis was passed on to the lower frequencies, where the signal strength is high and the measurement error low. Failing to do so lead to a refractive index calculation much lower than the measured value.

OSA CONTINUUM

The comparison between fit and measurement for the refractive index and absorption coefficient for the B_1 modes can be observed in Fig. 10 and for the B_2 modes in Fig. 11, respectively. The resonance frequencies and their associated damping coefficients and oscillator strength are shown in Tables 3 and 4, respectively.

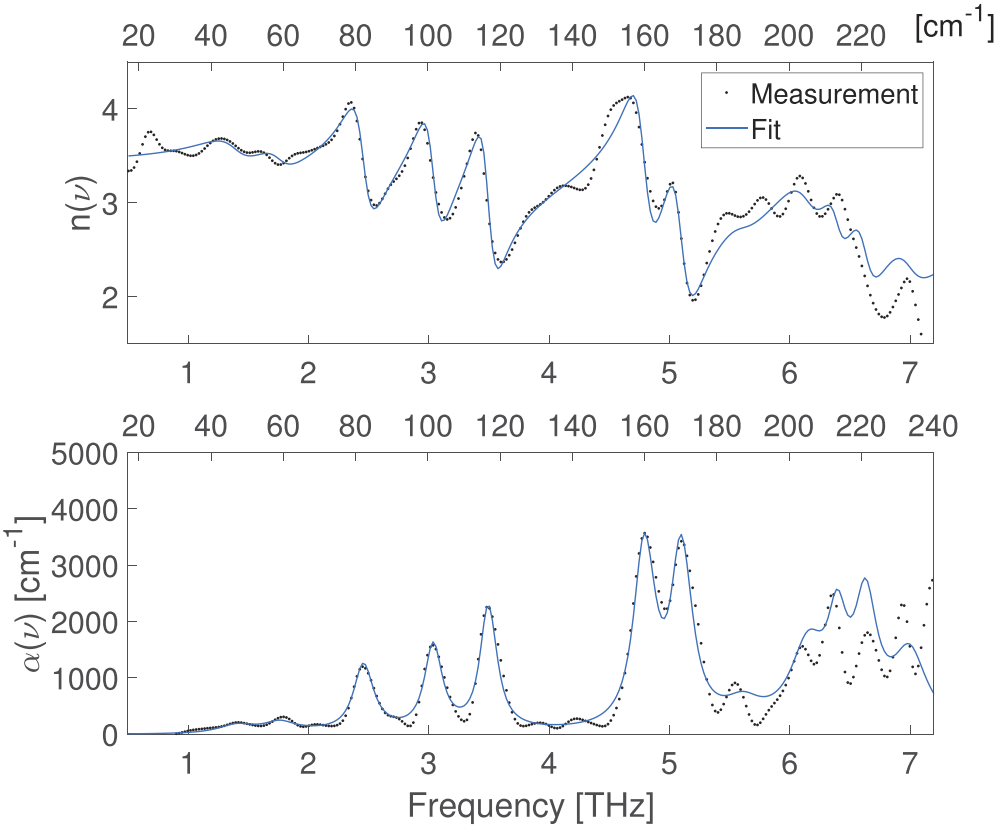

Fig. 10. Least squares fit (Eq. 6) for (TOP) the refractive index and (BOTTOM) absorption of B_1 modes using 16 resonances.

Many examples of Lorentzian resonance behaviour can be seen in this work, e.g. in Fig. 10 for the three peaks between 2 and 4 THz and the two peaks around 5 THz, where the absorption peak aligns well with the slope of the refractive index. In Fig. 11 we see similar behaviour around 2.7 and 3.7 THz. Some of the spectral features from Table 1 and 2 do not fit this behaviour, and might therefore not be Lorentzian in nature. This is evidenced by the fact that the fit estimates $\Delta\varepsilon = 0$ for some features, as well as a mismatch between data and fit in the region above 5 THz where the measurement error is largest.

The fits are qualitatively quite good but it is possible that some of the spectral features at lower frequencies would be better described by Debye behaviour. However, before the physical origin of these peaks have been decided a more elaborate fitting procedure seems premature.

OSA CONTINUUM

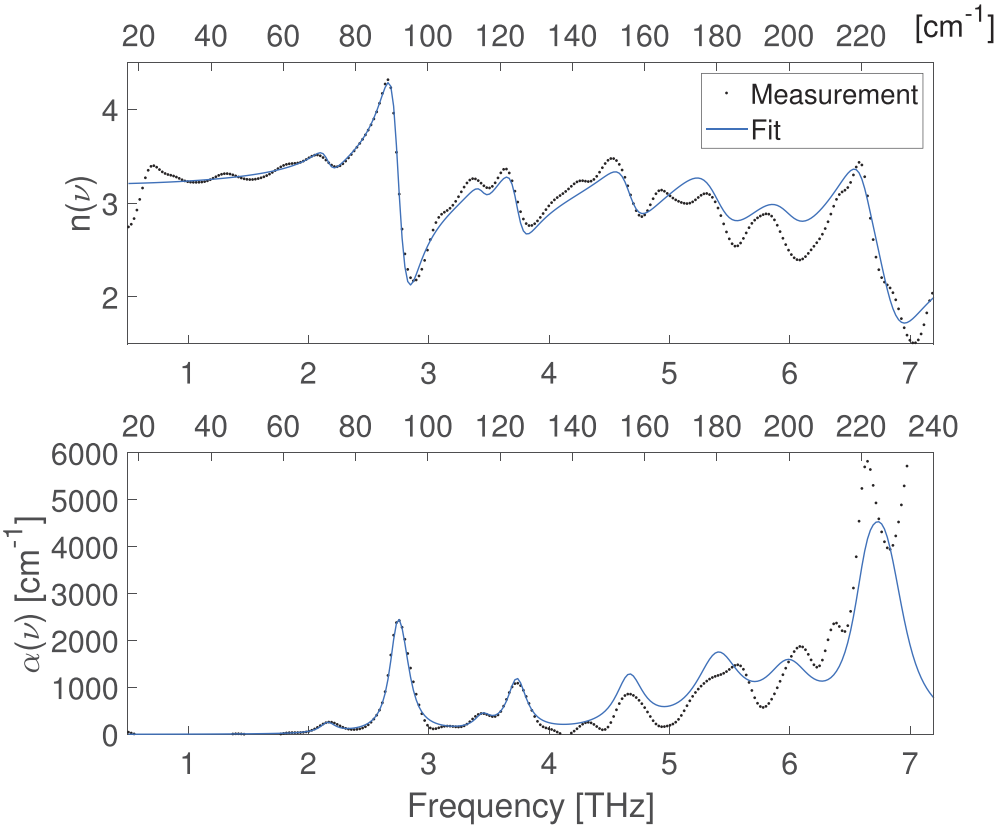

Fig. 11. Least squares fit (Eq. 6) for (TOP) the refractive index and (BOTTOM) absorption of B_2 modes using 12 resonances.

Table 3. Fitted peaks (Eq. 6) for the B_1 modes in KTP (ε_∞ = 7.51)

f_0 [cm^{-1}]	f_0 [THz]	$\Delta\varepsilon$	Γ
47.0000	1.4100	0.2801	1.3594
59.7667	1.7930	0.2936	1.9376
69.0000	2.0700	0.0161	0.4851
82.0000	2.4600	0.6491	1.2792
101.0000	3.0300	0.4493	1.0582
115.3000	3.4590	0.4200	0.9512
131.0000	3.9300	0.0116	2.3002
141.0000	4.2300	0.0000	2.7958
158.6700	4.7601	0.5168	1.2895
169.0000	5.0700	0.3128	1.2471
184.7667	5.5430	0.0354	0.8129
203.5000	6.1050	0.2214	2.9279
212.0000	6.3600	0.1852	2.0058
221.0000	6.6300	0.0973	1.2682
230.0000	6.9000	0.0938	2.2911
239.0000	7.1700	0.1007	2.2515

OSA CONTINUUM

Table 4. Fitted peaks (Eq. 6) for the B_2 modes in KTP (ε_∞ = 6.95)

f_0 [cm^{-1}]	f_0 [THz]	$\Delta\varepsilon$	Γ
62.0000	1.8600	0.0000	3.8222
72.0000	2.1600	0.0936	0.8007
90.7800	2.7234	0.8308	0.9589
105.0000	3.1500	0.0000	6.0188
114.0000	3.4200	0.0447	0.7027
123.8000	3.7140	0.2322	1.2713
144.0000	4.3200	0.0164	0.6033
155.0000	4.6500	0.1910	1.6282
185.5333	5.5660	0.6505	5.5893
203.0000	6.0900	0.0373	1.1634
212.0000	6.3600	0.0000	8.5564
221.5000	6.6450	0.5973	2.5496

4. Conclusion

We have performed reflection and transmission THz time-domain spectroscopy measurements on flux grown KTP. Our data is in good agreement with earlier results of differently grown samples measured with other techniques out to 240 cm^{-1}. We speculate that the differences between our work and others are mostly due to undocumented properties of the different samples. We have confirmed the observations in [16] of a peak close to 1.7 THz and a feature around 1 THz [16,34]. Additionally, we have observed a peak at approximately 1.4 THz. To our knowledge this peak has not been reported by others.

Funding

Knut och Alice Wallenbergs Stiftelse (501100004063).

Acknowledgement

The authors thank Erik Lysne, Hoon Jang and Ursula Gibson for fruitful discussions.

Disclosures

The authors declare no conflicts of interest.

References

1. M. Bibes, J. E. Villegas, and A. Barthélémy, "Ultrathin oxide films and interfaces for electronics and spintronics," Adv. Phys. **60**(1), 5–84 (2011).
2. A.-M. Haghiri-Gosnet and J.-P. Renard, "Cmr manganites: physics, thin films and devices," J. Phys. D: Appl. Phys. **36**(8), R127–R150 (2003).
3. J. A. Giordmaine and R. C. Miller, "Tunable coherent parametric oscillation in $LiNbO_3$ at optical frequencies," Phys. Rev. Lett. **14**(24), 973–976 (1965).
4. M. B. Klein and R. N. Schwartz, "Photorefractive effect in $BaTiO_3$: microscopic origins," J. Opt. Soc. Am. B **3**(2), 293 (1986).
5. J. D. Bierlein and C. B. Arweiler, "Electro-optic and dielectric properties of $KTiOPO_4$," Appl. Phys. Lett. **49**(15), 917–919 (1986).
6. J. D. Bierlein and H. Vanherzeele, "Potassium titanyl phosphate: properties and new applications," J. Opt. Soc. Am. B **6**(4), 622 (1989).
7. H. Karlsson and F. Laurell, "Electric field poling of flux grown $KTiOPO_4$," Appl. Phys. Lett. **71**(24), 3474–3476 (1997).

OSA CONTINUUM

8. S. Wang, V. Pasiskevicius, J. Hellström, F. Laurell, and H. Karlsson, "First-order type II quasi-phase-matched UV generation in periodically poled KTP," Opt. Lett. **24**(14), 978 (1999).
9. M. Pelton, P. Marsden, D. Ljunggren, M. Tengner, A. Karlsson, A. Fragemann, C. Canalias, and F. Laurell, "Bright, single-spatial-mode source of frequency non-degenerate, polarization-entangled photon pairs using periodically poled KTP," Opt. Express **12**(15), 3573–3580 (2004).
10. M. Fiorentino, S. M. Spillane, R. G. Beausoleil, T. D. Roberts, P. Battle, and M. W. Munro, "Spontaneous parametric down-conversion in periodically poled KTP waveguides and bulk crystals," Opt. Express **15**(12), 7479 (2007).
11. T. Zhong, F. N. Wong, T. D. Roberts, and P. Battle, "High performance photon-pair source based on a fiber-coupled periodically poled $KTiOPO_4$ waveguide," Opt. Express **17**(14), 12019 (2009).
12. C. W. Thiel, Y. Sun, R. M. Macfarlane, T. Böttger, and R. L. Cone, "Rare-earth-doped $LiNbO_3$ and $KTiOPO_4$ (KTP) for waveguide quantum memories," J. Phys. B: At., Mol. Opt. Phys. **45**(12), 124013 (2012).
13. T. Robin, C. Bouye, and J. Cochard, "Terahertz applications: trends and challenges," in *Terahertz, RF, Millimeter, and Submillimeter-Wave Technology and Applications VII*, L. P. Sadwick and C. M. O'Sullivan, eds. (SPIE, 2014).
14. H. A. Hafez, X. Chai, A. Ibrahim, S. Mondal, D. Férachou, X. Ropagnol, and T. Ozaki, "Intense terahertz radiation and their applications," J. Opt. **18**(9), 093004 (2016).
15. S. S. Dhillon, M. S. Vitiello, E. H. Linfield, A. G. Davies, M. C. Hoffmann, J. Booske, C. Paoloni, M. Gensch, P. Weightman, G. P. Williams, E. Castro-Camus, D. R. S. Cumming, F. Simoens, I. Escorcia-Carranza, J. Grant, S. Lucyszyn, M. Kuwata-Gonokami, K. Konishi, M. Koch, C. A. Schmuttenmaer, T. L. Cocker, R. Huber, A. G. Markelz, Z. D. Taylor, V. P. Wallace, J. A. Zeitler, J. Sibik, T. M. Korter, B. Ellison, S. Rea, P. Goldsmith, K. B. Cooper, R. Appleby, D. Pardo, P. G. Huggard, V. Krozer, H. Shams, M. Fice, C. Renaud, A. Seeds, A. Stöhr, M. Naftaly, N. Ridler, R. Clarke, J. E. Cunningham, and M. B. Johnston, "The 2017 terahertz science and technology roadmap," J. Phys. D: Appl. Phys. **50**(4), 043001 (2017).
16. V. D. Antsygin, A. B. Kaplun, A. A. Mamrashev, N. A. Nikolaev, and O. I. Potaturkin, "Terahertz optical properties of potassium titanyl phosphate crystals," Opt. Express **22**(21), 25436 (2014).
17. A. Mamrashev, N. Nikolaev, V. Antsygin, Y. Andreev, G. Lanskii, and A. Meshalkin, "Optical properties of KTP crystals and their potential for terahertz generation," Crystals **8**(8), 310 (2018).
18. P. Zeil, "Tailored fiber lasers and their use in nonlinear optics," Ph.D. thesis, KTH, Laser Physics (2015).
19. P. Zeil, V. Pasiskevicius, and F. Laurell, "Tunable, high-power, continuous-wave dual-polarization Yb-fiber oscillator," Opt. Express **23**(13), 17450–17455 (2015).
20. M.-H. Wu, Y.-C. Chiu, T.-D. Wang, G. Zhao, A. Zukauskas, F. Laurell, and Y.-C. Huang, "Terahertz parametric generation and amplification from potassium titanyl phosphate in comparison with lithium niobate and lithium tantalate," Opt. Express **24**(23), 25964 (2016).
21. M.-H. Wu, W.-C. Tsai, Y.-C. Chiu, and Y.-C. Huang, "Generation of ~ 100 kw narrow-line far-infrared radiation from a ktp off-axis thz parametric oscillator," Optica **6**(6), 723–730 (2019).
22. P. I. Tordjman, E. Masse, and J. C. Guitel, "Structure cristalline du monophosphate $KTiPO_5$," Z. Kristallogr. **139**(1-2), 103–115 (1974).
23. S. Dezhong and H. Chaoen, "A new nonlinear optical crystal KTP," Prog. Cryst. Growth Charact. **11**(4), 269–274 (1985).
24. G. D. Stucky, M. L. F. Phillips, and T. E. Gier, "The potassium titanyl phosphate structure field: a model for new nonlinear optical materials," Chem. Mater. **1**(5), 492–509 (1989).
25. P. A. Thomas, A. M. Glazer, and B. E. Watts, "Crystal structure and nonlinear optical properties of $KSnOPO_4$ and their comparison with $KTiOPO_4$," Acta Crystallogr., Sect. B: Struct. Sci. **46**(3), 333–343 (1990).
26. N. I. Sorokina and V. I. Voronkova, "Structure and properties of crystals in the potassium titanyl phosphate family: A review," Crystallogr. Rep. **52**(1), 80–93 (2007).
27. A. H. Reshak, I. V. Kityk, and S. Auluck, "Investigation of the linear and nonlinear optical susceptibilities of $KTiOPO_4$ single crystals: Theory and experiment," J. Phys. Chem. B **114**(50), 16705–16712 (2010).
28. B. Boulanger, J. P. Fève, G. Marnier, B. Ménaert, X. Cabirol, P. Villeval, and C. Bonnin, "Relative sign and absolute magnitude of $d^{(2)}$ nonlinear coefficients of KTP from second-harmonic-generation measurements," J. Opt. Soc. Am. B **11**(5), 750–757 (1994).
29. B. Wyncke, F. Brehat, J. Mangin, G. Marnier, M. F. Ravet, and M. Metzger, "Infrared reflectivity spectrum of $KTiOPO_4$ single crystal," Phase Transitions **9**(2), 179–183 (1987).
30. G. E. Kugel, F. Brehat, B. Wyncke, M. D. Fontana, G. Marnier, C. Carabatos-Nedelec, and J. Mangin, "The vibrational spectrum of a $KTiOPO_4$ single crystal studied by raman and infrared reflectivity spectroscopy," J. Phys. C: Solid State Phys. **21**(32), 5565–5583 (1988).
31. B. Mohamadou and G. E. Kugel, "Raman scattering from polar modes in $KTiOPO_4$ single crystals," Phys. Status Solidi B **195**(1), 97–111 (1996).
32. K. Vivekanandan, S. Selvasekarapandian, P. Kolandaivel, M. Sebastian, and S. Suma, "Raman and FT-IR spectroscopic characterisation of flux grown $KTiOPO_4$ and $KRbTiOPO_4$ non-linear optical crystals," Mater. Chem. Phys. **49**(3), 204–210 (1997).
33. G. H. Watson, "Polarized raman spectra of $KTiOAsO_4$ and isomorphic nonlinear-optical crystals," J. Raman Spectrosc. **22**(11), 705–713 (1991).
34. P. Mounaix, L. Sarger, J. Caumes, and E. Freysz, "Characterization of non-linear potassium crystals in the terahertz frequency domain," Opt. Commun. **242**(4-6), 631–639 (2004).

OSA CONTINUUM

35. S. Mei, F. Liang, L. Xin-Chao, and Z. Wei-Li, "Optical phonon resonance of $KTiOPO_4$ crystal characterized by THz time-domain spectroscopy," Acta Photonica Sinica **38**, 1344 (2009).
36. A. Card, M. Mokim, and F. Ganikhanov, "Resolving fine spectral features in lattice vibrational modes using femtosecond coherent spectroscopy," AIP Adv. **6**(2), 025115 (2016).
37. H. Hamster, A. Sullivan, S. Gordon, W. White, and R. W. Falcone, "Subpicosecond, electromagnetic pulses from intense laser-plasma interaction," Phys. Rev. Lett. **71**(17), 2725–2728 (1993).
38. D. J. Cook and R. M. Hochstrasser, "Intense terahertz pulses by four-wave rectification in air," Opt. Lett. **25**(16), 1210–1212 (2000).
39. A. Pashkin, M. Kempa, H. Němec, F. Kadlec, and P. Kužel, "Phase-sensitive time-domain terahertz reflection spectroscopy," Rev. Sci. Instrum. **74**(11), 4711–4717 (2003).
40. "Contact moelster@kth.se for the raw data.".
41. P. U. Jepsen and B. M. Fischer, "Dynamic range in terahertz time-domain transmission and reflection spectroscopy," Opt. Lett. **30**(1), 29–31 (2005).
42. K. Mølster, "THz time domain spectroscopy of materials in reflection and transmission," Master's thesis, Department of Electronic Systems, Faculty of Information Technology and Electrical Engineering, NTNU (2017).
43. J. M. Fornies-Marquina, J. Letosa, M. Garcia-Gracia, and J. M. Artacho, "Error propagation for the transformation of time domain into frequency domain," IEEE Trans. Magn. **33**(2), 1456–1459 (1997).
44. J.-L. Coutaz, F. Garet, and V. Wallace, *Principles of Terahertz Time-Domain Spectroscopy* (Jenny Stanford Publishing, 2018).
45. C. Canalias, J. Hirohashi, V. Pasiskevicius, and F. Laurell, "Polarization-switching characteristics of flux-grown $KTiOPO_4$ and $RbTiOPO_4$ at room temperature," J. Appl. Phys. **97**(12), 124105 (2005).
46. M. Rüsing, C. Eigner, P. Mackwitz, G. Berth, C. Silberhorn, and A. Zrenner, "Identification of ferroelectric domain structure sensitive phonon modes in potassium titanyl phosphate: A fundamental study," J. Appl. Phys. **119**(4), 044103 (2016).